Investigation of $Nd_xY_{0.25-x}Zr_{0.75}O_{1.88}$ Inert Matrix Fuel Materials Made by a Co-Precipitation Synthetic Route

John R. Hayes, Andrew P. Grosvenor*
Department of Chemistry, University of Saskatchewan, Saskatoon, SK, S7N 5C9

*Author to whom correspondence should be addressed
E-mail: andrew.grosvenor@usask.ca
Phone: (306) 966-4660
Fax: (306) 966-4730

Abstract

Yttria-substituted zirconia is a material that is being considered for use as an inert matrix fuel in nuclear reactors, but a complete characterization of these materials is required for them to be licensed for use. A series of $Nd_xY_{0.25-x}Zr_{0.75}O_{1.88}$ materials have been synthesized using a co-precipitation method, and the thermal stability of these materials has been studied by annealing them at 1400 °C and 1500 °C. (Nd was used as surrogate for Am). The long-range and local structures of the materials were characterized via powder X-ray diffraction, scanning electron microscopy, wavelength dispersive spectroscopy, and X-ray absorption spectroscopy at the Zr and Y K-edges. These results were compared with the previous characterization of Nd-YSZ materials synthesized using a ceramic method. The results indicated that the ordering in the local metal-oxygen polyhedral remains relatively unaffected by synthetic method, but there was increased long-range disorder in the materials prepared by the co-precipitation method. Further, it was found that the materials produced by the co-precipitation method were unexpectedly unstable when annealed at high temperature. This study highlights the importance of determining the effect of synthetic method on material properties and demonstrates how the co-precipitation route could be used to produce IMFs.

Keywords: XAS, ceramics, stabilized zirconia, nuclear energy, XRD

1. Introduction

World energy demands continue to increase as the world becomes more industrialized, while climate change is dictating that this energy be produced with relatively low carbon emissions.[1–3] Nuclear energy is a proven means to generate vast quantities of electricity while producing minimal lifetime carbon emissions.[3,4] However, nuclear power generates radiotoxic waste that must be stored securely for thousands of years.[5,6] Spent nuclear fuel must be stored for long periods of time due to the presence of transuranic species (TRUs; i.e., Pu, Np, Am, Cm), which account for the majority of the fuel radiotoxicity after several hundred years.[7–9] These TRU elements could be eliminated by "burning up" (i.e., transmuting) the elements in commercial nuclear reactors, and inert matrix fuels (IMFs) have been proposed as a means for burning up TRU elements in current generation reactors.[7,9–12]

An IMF consists of TRU elements embedded in a neutron transparent (inert) material. Cubic zirconia (ZrO_2), which adopts the fluorite structure, has often been proposed for use as IMFs due to its low neutron cross-section, chemical durability, and resistance to radiation damage.[13–16] Further, cubic zirconia has the added benefit of being a viable long-term storage material, which would allow for direct storage of the spent nuclear fuel without the need for further reprocessing.[13,17,18] However, pure cubic zirconia is not stable at temperatures below 2370 °C, adopting a tetragonal structure between 1170 – 2370 °C and a monoclinic structure below 1170 °C.[19–22] The tetragonal and monoclinic structures are formed by distorting the cubic fluorite structure.[23–26]

The cubic structure can be stabilized by adding an aliovalent cation, and Y^{3+} has been commonly used as the dopant ion.[22,27–30] The size difference between Y^{3+} and Zr^{4+} as well as oxygen vacancies generated by charge balancing requirements act to stabilize the fluorite structure.[19,31] In doped cubic zirconia systems, the dopant and Zr are randomly distributed in the Zr 4a site. [19,31] The depth of knowledge regarding yttria-stabilized zirconia (YSZ) is large, and YSZ materials have been studied extensively for use in a wide variety of applications, including solid-oxide fuel cells, refractory material applications, and structural wear components.[14,20,32–36] However, research to determine how the material properties are impacted by adding TRU species to YSZ remains relatively rare. It is necessary to understand how stability of the fluorite structure of YSZ is impacted by the addition of TRU elements, as there is an increase in volume and a decrease in thermal conductivity accompanying

the transition from fluorite to a lower symmetry phase.[16,20,32,37,38] These changes are undesirable and could lead to fuel failure conditions.

Our group has previously studied the thermal stability of a number of $Nd_xY_yZr_{1-x-y}O_{2-\delta}$ materials made by the ceramic method.[39] (Nd was used as a surrogate for Am.) However, Nd was not evenly distributed in these materials, and it is therefore of interest to investigate if the Nd distribution can be improved using alternate synthetic techniques.[39] Further, ceramic synthesis is generally costly, and the presence of powdered radioactive material would make large scale syntheses envisioned for safe nuclear fuel production difficult.[40] A low-temperature, liquid-based approach could be more easily automated as well, reducing the costs of safely producing nuclear fuels bearing TRU species.[40] A series of $Nd_xY_{0.25-x}Zr_{0.75}O_{1.88}$ materials have been produced in the current study using a co-precipitation method, followed by calcining at 800 °C. These "as-synthesized" materials were then annealed at 1400 °C and 1500 °C to explore the effect of high temperature annealing on the thermal stability of Nd-doped yttria-stabilized zirconia made by the co-precipitation method. The local and long-range structures of these materials have been investigated using powder X-ray diffraction (XRD), scanning electron microscopy (SEM), and X-ray absorption spectroscopy (XAS). These results were compared to similar results from Nd-YSZ materials made via a ceramic method reported previously.[39] This study has shown that the local bonding structures around the metal centres in the materials made by the co-precipitation synthesis method or the ceramic synthesis method are similar. However, the intermediate and long-range structures of the materials made by the co-precipitation method were more disordered compared to the structures of the materials made by the ceramic method. Finally, this study has also shown that cubic $Nd_xY_{0.25-x}Zr_{0.75}O_{1.88}$ materials made by a co-precipitation method are less stable compared to Nd-YSZ materials made by the ceramic method. This study highlights the importance of synthetic method and the impacts it can have on the properties of zirconia-based inert matrix fuels.

2. Experimental

2.1. Preparation of $Nd_xY_{0.25-x}Zr_{0.75}O_{1.88}$ materials

$Nd_xY_{0.25-x}Zr_{0.75}O_{1.88}$ materials were prepared via co-precipitation using an adaptation of a previously reported synthetic method.[41] Nd_2O_3 (Alfa Aesar, 99.9%) and Y_2O_3 (Alfa Aesar, 99.99%) were dissolved in boiling

nitric acid while $ZrOCl_2 \cdot 8H_2O$ (Alfa Aesar, 99.9%) was dissolved in deionized water at room temperature. The boiling Nd^{3+}/Y^{3+} solution was added to the room temperature Zr^{4+} solution and room temperature concentrated ammonia was added which resulted in the formation of a precipitate. The solid was collected via vacuum filtration, washed with deionized water to remove counter-ions and excess ammonia, and dried in air at 110 °C for 24 h. The dried precipitate was then calcined as a free powder at 800 °C for 24 h, resulting in the final product. These materials are referred to as the "as-synthesized" samples in this article. Aliquots of the as-synthesized materials were then annealed at 1400 °C and 1500 °C as free powders for 24 hours. The $Nd_xY_{0.25-x}Zr_{0.75}O_{1.88}$ materials prepared by the ceramic method using binary metal oxides as reactants were synthesized for a previous study, and the full experimental details of the synthesis of these materials have been previously described.[39]

The phase identification of the as-synthesized and annealed materials was performed using powder XRD. The powder XRD patterns were collected using a PANalytical Empyrean diffractometer using either Cu $K_{\alpha 1,2}$ (λ=1.5406 Å) or Co $K_{\alpha 1,2}$ (λ=1.7890 Å) radiation. Phase quantification was obtained by Rietveld refinement using the PANalytical X'pert HighScore Plus software program.[42] Rietveld refinements were performed by fitting cubic ZrO_2, tetragonal ZrO_2, and monoclinic ZrO_2 phases to the data.[43–45] The phases used to model the diffraction data were adapted from the pure ZrO_2 patterns by adding Nd and Y to the crystallographic site occupied by Zr. The site occupancies were set to be consistent with the ideal stoichiometry of each material. For example, the cubic ZrO_2 pattern for the $Nd_{0.10}Y_{0.15}Zr_{0.75}O_{1.88}$ pattern was generated by adding Nd and Y to the Zr 4a site. The Zr site occupancy was set to 0.75 while the Nd site occupancy was set to 0.10 and the Y site occupancy was set to 0.15. The addition of Y and Nd impacted the intensity of the modelled peaks and improved the quality of the fits. The background was fitted using a 3rd order polynomial function which also included a 1/2θ term.

2.2. SEM and WDS analysis

Scanning electron micrographs were collected from several of the as-synthesized and annealed samples using a JEOL 8600 electron microprobe. Samples were prepared by pressing ~0.125 g of the as-synthesized material into a pellet at 8 MPa, and sintering the pellet at 800 °C for 24 h; these are referred to as the "as-synthesized" pellets. After sintering, several of the "as-synthesized" pellets were further annealed at 1400 °C for 24 h; these pellets are referred to as the annealed pellets. The pellets were mounted in a plastic disk using a polymer resin, and the surface of the sample disk was polished to a smooth surface using diamond paste. The

surface was coated with a thin C film to reduce charging effects before being inserted into the microprobe sample chamber. All electron micrographs were collected in backscattered electron mode, and the electron beam accelerating voltage was 20 keV.

Wavelength dispersive spectroscopy (WDS) was also performed to collect elemental distribution maps. The electron beam accelerating voltage was 20 keV and the probe current was 50 nA. The peak counting times were 60 s on peak and 30 s each on high and low background. The X-ray maps were collected using the Nd L_α and Y L_α signals measured simultaneously using two different WDS spectrometers. The WDS spectrometers were tuned to the correct fluorescence energy using the fluorescence signals from (Nd,Ce)PO_4 (Nd $L_{\alpha 1}$) and Y_2O_3 (Y $L_{\alpha 1}$) standards. All X-ray maps were collected at the same magnification and from the same region as the electron micrographs.

2.3. Zr K- and Y K-edge X-ray Absorption Spectroscopy

Zr K- and Y K-edge X-ray absorption spectra were collected using the CLS@APS Sector 20 Bending Magnet beamline at the Advanced Photon Source (APS) located at Argonne National Laboratories. A silicon (111) double crystal monochromator with a Rh harmonic rejection mirror was used, which has a resolution of 2.5 eV at 18000 eV (Zr K-edge), and the beamline flux was ~10^{11} photons/s.[46] The samples were prepared by applying the finely ground powders between layers of Kapton tape and adjusting the number of layers to provide optimal absorption. The samples were mounted at 45° to the incident beam and spectra were collected in both transmission and partial fluorescence yield (PFY) mode. The incident beam ion chamber (I_o) was filled with $N_{2(g)}$ while the transmitted beam ion chamber, I_T, and reference ion chamber, I_{REF}, were filled with an 80% $Ar_{(g)}$:20% $N_{2(g)}$ mixture. A Canberra 13 element Ge fluorescence detector was used to record the PFY signal.

The XANES region of the Zr K- and Y K-edge spectra were collected using a 0.3 eV step through the edge. The Zr K- and Y K-edge spectra were calibrated using a Zr metal foil, having a known edge energy of 17998 eV.[47] The metal foil was measured in-line when collecting the Zr K-edge spectra. The spectrum from the Zr metal foil was measured separately when collecting the Y K-edge spectra. The Extended X-ray Absorption Fine Structure (EXAFS) spectra were collected to k = 15 with a 0.05 k step size.

The EXAFS spectra were analyzed by fitting the parameters of the standard EXAFS equation:

$$\chi(k) = \sum_j \frac{N_j S_o^2}{kR_j^2} F_j(k) e^{-2\sigma_j^2 k^2} e^{-2R_j/\lambda} \sin\left(2kR_j + \phi_j(k)\right)$$

where N_j is the number of j^{th} atoms at a distance R_j from the absorbing atomic centre, $F_j(k)$ is the backscattering function, σ_j^2 is the Debye-Waller Factor, and $\phi_j(k)$ is the phase-shift function of the jth atom.[48] These parameters are described in detail in previous publications.[39,48] The Zr K-edge EXAFS spectra were analyzed by calculating $F_j(k)$, $\phi_j(k)$, and λ for each set of scattering pairs in a given cluster using the FEFF6 code.[49] The Zr–Zr and Zr–Y paths were considered as equivalent, due to the similar atomic number of Zr and Y. The other parameters were fit using a least-squares refinement as described below using the Artemis program, which is included in the Demeter software suite.[50]

The scattering cluster for the FEFF calculation was generated from a cubic zirconia model using the lattice parameter determined from the powder XRD analysis. Nd was manually doped into the next nearest neighbor shells. It has been previously determined that the FEFF calculations were not affected by the substitution position of the Nd atom.[39] The Zr K-edge spectra were fitted as follows. The first shell Zr–O, second shell Zr–Zr/Y and Zr–Nd, and third shell Zr–O (denoted as Zr–O2) scattering paths were included in the fitting model. The coordination number (CN) of each scattering path was set manually to reflect the stoichiometry of the sample and then varied as necessary to improve fits. The E_o and S_o^2 parameters were fitted as a global variable across all scattering paths. Individual Debye-Waller and ΔR factors were for each single-scattering path. The Zr–O–Zr/Y and Zr–O–Nd multiscattering paths were also included in the model. The Debye-Waller factors were calculated as $2*\sigma^2_{Zr-O}+\sigma^2_{Zr-Zr}$ and $2*\sigma^2_{Zr-O}+\sigma^2_{Zr-Nd}$, respectively. The ΔR parameters were calculated to be $2*\Delta R_{Zr-O}+ \Delta R_{Zr-Zr}$. The Y K-edge spectra were fitted in a similar manner, except that Y was used as the central atom in the scattering cluster. All other details of the fitting model were identical to the Zr K-edge analysis.

3. Results and Discussion

3.1. Powder XRD

The powder X-ray diffraction patterns from the as-synthesized and annealed $Nd_xY_{0.25-x}Zr_{0.75}O_{1.88}$ materials synthesized via a co-precipitation method are presented in Figures 1 and 2 and Figure S1. Only peaks associated with the cubic fluorite phase were observed in the as-synthesized materials. The diffraction peaks were sharper in

the materials annealed at high temperature compared to the diffraction peaks from the materials calcined at 800 °C, indicating that the crystallinity of the materials improved upon annealing. Several of the compositions annealed at high temperature were not phase pure, and lower symmetry monoclinic and tetragonal ZrO_2, in addition to an unidentified phase, were observed (Figure 1a, Figure 2).

Phase analysis was performed using Rietveld refinement and the results of these fits are given in Table 1. The $Nd_xY_{0.25-x}Zr_{0.75}O_{1.88}$ materials prepared by the co-precipitation method with $x \leq 0.15$ that were annealed at high temperatures were phase pure, and only peaks associated with the fluorite structure were observed (Figure 1b, Figure S1). When $Nd_{0.20}Y_{0.05}Zr_{0.75}O_{1.88}$ made by the co-precipitation method was annealed at 1400 °C, minor contributions from monoclinic (4.0 %) and tetragonal (3.4%) ZrO_2 phases were observed. Peaks associated with an unidentified phase were also observed when the $Nd_{0.20}Y_{0.05}Zr_{0.75}O_{1.88}$ material made by co-precipitation was annealed at 1500 °C (Figure 1a). Monoclinic (24.7%) and tetragonal (3.6 %) ZrO_2 phases were observed when the $Nd_{0.25}Zr_{0.75}O_{1.88}$ sample synthesized via the co-precipitation method was annealed at 1400 °C (Figure 2a). When this material was annealed at 1500 °C the amount of monoclinic and tetragonal ZrO_2 present decreased, and the Rietveld analysis indicated that the material contained 14.5% monoclinic ZrO_2. This result is expected, as ternary phase diagrams of the Nd_2O_3-Y_2O_3-ZrO_2 systems have shown that the cubic fluorite structure is stable across a wider range of compositions at higher temperatures (1600 °C) than at lower temperatures (1400 °C).[35]

These results differ from the results of the powder XRD analysis for $Nd_xY_{0.25-x}Zr_{0.75}O_{1.88}$ materials prepared by the ceramic method.[39] $Nd_{0.20}Y_{0.05}Zr_{0.75}O_{1.88}$ made via the ceramic route at 1500 °C was phase pure, and no unidentified peaks were observed in the powder XRD pattern, and no impurity phases were observed when $Nd_{0.20}Y_{0.05}Zr_{0.75}O_{1.88}$ made by the ceramic method was annealed at 1400 °C.[39] Only the fluorite phase was observed in the $Nd_{0.25}Zr_{0.75}O_{1.88}$ material made via the ceramic method at 1500 °C.[39] Similar to $Nd_{0.25}Zr_{0.75}O_{1.88}$ made by the co-precipitation method, the material made by the ceramic synthesis was also observed to decompose to lower symmetry phases upon annealing at 1400 °C, though the degree of decomposition was much less when compared to the material made by a co-precipitation route (Figure 2b).[39] Again, decomposition to a lower symmetry phase upon annealing is expected based on the calculated Nd_2O_3-Y_2O_3-ZrO_2 ternary phase diagrams; however, it was not expected that the degree of decomposition the materials would be dependent on synthetic

method. [35] In all cases, no superstructural peaks associated with a pyrochlore phase were observed, indicating that the oxygen vacancies were not significantly ordered on a long-range scale within the material.

The results presented above indicate that the fluorite structure is more stable for the materials made by the ceramic synthetic route than by the co-precipitation route. This stability is likely driven by the kinetics of the cubic to tetragonal ZrO_2 and cubic to monoclinic ZrO_2 phase transitions, which are controlled by the diffusion of cations within the matrix.[51–54] In the case of the co-precipitation synthesis, the cations are already intimately mixed at an atomic level, facilitating a faster reaction. This is evident by the difference in the annealing times required to induce phase changes, which were much shorter in the case of the co-precipitation route (24 h) as compared to the materials made by the ceramic route (5 d). These results suggest that the kinetically labile materials made by the co-precipitation method may have reached a thermodynamically favorable endpoint upon annealing. These results also suggest that there is a possibility that while the fluorite structure of the $Nd_{0.20}Y_{0.05}Zr_{0.75}O_{1.88}$ material made by the ceramic route was stable when annealed at 1400 °C for 5 d, it may not be stable when annealed at 1400 °C for extended periods of time.[39] Further annealing studies, using much longer heating times, should be performed to explore this possibility fully.

The lattice constants of the as-synthesized and annealed $Nd_xY_{0.25-x}Zr_{0.75}O_{1.88}$ materials made by the co-precipitation and ceramic syntheses were determined by Rietveld refinement (Table 1), and the lattice constants are plotted as a function of Nd content in Figure 3. The lattice constants of the as-synthesized materials synthesized by both the co-precipitation and ceramic methods varied linearly with Nd content (x), consistent with Vegard's law.[55] The lattice constants of all the as-synthesized and annealed materials synthesized via co-precipitation were less than the lattice constants of the materials synthesized by the ceramic method. The lattice constants of the materials synthesized by the co-precipitation method increased when they were annealed at 1400 °C and 1500 °C, which resulted in deviations from Vegard's law. The magnitude of the change in the lattice constants induced by annealing at high temperature decreased with increased Nd content when "x" in the chemical formula was less than 0.10. Conversely, the magnitude of the change in the lattice constant caused by annealing increased as the Nd content increased when x was greater than 0.10. The lattice constant of the materials annealed at 1500 °C were lower than the lattice constants of the materials annealed at 1400 °C when x = 0.20 and x = 0.25. It should also be noted that at higher Nd concentrations, the changes in the phase composition,

which are driven by Nd segregation within the material (see Section 3.2), likely affect the lattice constant of the fluorite structure.

It has been previously suggested that the fluorite lattice constant is affected by ordering of the metal-oxygen polyhedral units.[36] Put another way, this means that the unit cell is affected by how the metal-oxygen polyhedra are arranged, rather than by variations in the local metal-oxygen bond lengths and angles.[36] The lattice constant is expected to increase as arrangement of the metal-oxygen polyhedra becomes more ordered, resulting in less efficient packing of the metal-oxygen polyhedral units.[36] The changes in the lattice constants observed here suggest that there was more long-range *disorder* in the as-synthesized materials made by the co-precipitation route compared to the materials synthesized by the ceramic method and the materials synthesized by co-precipitation method that were annealed at high temperature. In the case of the ceramic synthetic route, this ordering may derive from both the high temperature at which the materials were annealed and also the inherent crystallinity of the starting materials. The starting binary oxides used in the ceramic route had defined crystal structures, which likely acted as a template, increasing the ordering between the metal-oxygen polyhedra.[56] In contrast, the starting precipitate materials that were formed in the co-precipitation method lacked this inherent structure. This explains why the lattice constants of the materials made via the ceramic method were greater than the materials made via the co-precipitation route.

3.2. SEM and WDS

The SEM micrographs and Nd and Y X-ray maps collected from the as-synthesized and annealed $Nd_{0.20}Y_{0.05}Zr_{0.75}O_{1.88}$ and $Y_{0.25}Zr_{0.75}O_{1.88}$ materials prepared by the co-precipitation route are presented in Figures 4 and 5. The micrographs from the as-synthesized samples (Figures 4a, 5a) show that the surfaces of the pellets contained large, faceted grains, and that the surfaces were similar to the previously reported surfaces of $Nd_xSc_yZr_{1-x-y}O_{2-\delta}$ pellets that were also synthesized using a co-precipitation method and annealed at 800 °C.[57] The surfaces became less faceted and more porous upon annealing at 1400 °C (Figures 4b, 4c). The topography of the surfaces of the pellets annealed at 1400 °C were similar to the surfaces of $Nd_xY_yZr_{1-x-y}O_{2-\delta}$ pellets prepared by the ceramic method.[39] An identical change in topography was also observed by SEM when $Nd_xSc_yZr_{1-x-y}O_{2-\delta}$ materials

made via co-precipitation were annealed at 1400 °C.[57] This indicates that the surface topography depends significantly on annealing temperature, with material composition and synthetic method playing little to no role.

The Y Kα X-ray maps (Figures 4b,d and Figures 5c,f) show that Y was evenly distributed throughout the material in both the as-synthesized and annealed $Nd_{0.20}Y_{0.05}Zr_{0.75}O_{1.88}$ and $Y_{0.25}Zr_{0.75}O_{1.88}$ materials made using the co-precipitation route. A similar result was observed in materials made via the ceramic method.[39] The Nd Lα X-ray maps (Figures 5b,e) indicated that Nd was evenly distributed in the as-synthesized $Nd_{0.20}Y_{0.05}Y_{0.75}O_{1.88}$ material made by the co-precipitation method. However, small Nd bright spots were detected when this material was annealed at 1400 °C. Nd bright spots were also observed when the $Nd_xY_{0.25-x}Zr_{0.75}O_{1.88}$ materials made by the ceramic method were annealed at 1400 °C as well.[39] The X-ray maps indicated that Y and Nd were evenly distributed in the as-synthesized $Nd_xY_{0.25-x}Zr_{0.75}O_{1.88}$ materials made by the co-precipitation method, and that Nd became segregated while Y remained homogenously distributed within the materials upon annealing at high temperature (Figures 4 and 5).

3.3. Zr K-edge XAS

3.3.1. XANES

Zr K-edge XANES spectra were collected from the as-synthesized and annealed samples prepared by the co-precipitation method, and the spectra are presented in Figure 6 and Figure S2. Three features were observed in the spectra, and are labelled A, B, and B' in Figure 6a. Feature A comprises the pre-edge and results from Zr 1s → 4d transitions while features B and B' comprise the main-edge and result from Zr 1s → 5p excitations.[58,59] The Zr K-edge spectra do not vary significantly as Nd replaces Y in the system. This result indicates that the local Zr coordination environment does not change with composition, which is consistent with our previously reported analysis of $Nd_xY_yZr_{1-x-y}O_{2-\delta}$ materials prepared by the ceramic method.[39]

The Zr K-edge spectra from the materials prepared by the co-precipitation method and annealed at high temperature are compared in Figure 6b. Changes in the spectra were only observed when the $Nd_{0.25}Zr_{0.75}O_{1.88}$ material was annealed at 1400 °C and 1500 °C (*Inset*, Figure 6b). When $Nd_{0.25}Zr_{0.75}O_{1.88}$ made by the co-precipitation method was annealed at 1400 °C, the energy separation between features B and B' decreased and there was an increase in intensity of the spectrum at ~18020 eV. This change has previously been shown to

correspond to a transition to lower symmetry ZrO_2, and is consistent with the powder XRD results (*vide supra*).[39] The spectrum from the $Nd_{0.25}Zr_{0.75}O_{1.88}$ material annealed at 1500 °C was similar to the spectrum from the as-synthesized material, though a decrease in the energy separation between features B and B' was still observed. This change indicates that lower symmetry ZrO_2 was still present in the system, but not to the degree that was observed in the $Nd_{0.25}Zr_{0.75}O_{1.88}$ material annealed at 1400 °C, which is also consistent with the powder XRD results. No changes in the Zr K-edge spectra were observed when any of the other $Nd_xY_{0.25-x}Zr_{0.75}O_{1.88}$ materials made by the co-precipitation method were annealed at high temperatures.

The Zr K-edge spectra from the as-synthesized and annealed $Nd_xY_{0.25-x}Zr_{0.75}O_{1.88}$ samples made by the co-precipitation method are compared to spectra from the as-synthesized materials made by the ceramic synthetic route in Figure 6c and Figure S2.[39] The intensity of feature A is slightly greater in the spectra collected from the materials made by the ceramic route compared to the intensity of feature A in the spectra from the materials made by the co-precipitation route. The pre-edge region is strongly affected by changes in coordination number as breaks in inversion symmetry around the metal centre result in p-d mixing, which increases the dipole character of the forbidden quadrapolar transition. Here, this likely indicates that the coordination number of Zr is lower in the materials made by the ceramic route than by the co-precipitation route. Changes in the intensities of features B and B' were observed between the spectra from the materials made by co-precipitation and the materials made by a ceramic method, and the intensity of feature B' is greater in the spectra from the materials made by the ceramic method compared to the intensity of feature B' in the spectra from the materials made by the co-precipitation method. The intensity of feature B in the spectra from the materials made by the ceramic method compared to the intensity of feature B in the spectra from the materials made by the co-precipitation method. These changes are consistent with the changes in the pre-edge, and are indicative of a change in the Zr CN number.[58,59] Overall, these results indicate the Zr coordination environment in the quaternary $Nd_xY_{1-x}Zr_{0.75}O_{1.88}$ materials was not affected by changes in composition or thermal treatment; however, the Zr coordination environment *was* observed to be dependent on the synthetic route used.

3.3.2. EXAFS

The Fourier transformed Zr K-edge EXAFS spectra were collected from the $Nd_xY_{0.25-x}Zr_{0.75}O_{1.88}$ materials made using the co-precipitation method, and these are presented in Figure 7 and Figure S3. Two major features,

labelled C and D in Figure 7a, were observed in the spectra. Feature C is attributed to the first shell Zr–O scattering path and feature D arises due to the second shell Zr–Zr, Zr–Y, and Zr–Nd scattering paths.[27,36,39] The intensity of feature C changes slightly with composition, though these changes do not appear to have a general trend and are likely observed due to noise within the data. The intensity of feature D decreased as the Nd content increased. The cause for the change is related to interference between the Zr–Zr/Y scattering paths and the Zr–Nd paths; the origin of this phenomenon has been previously described.[39]

The intensities of features C and D increased when all of the materials prepared by the co-precipitation route were annealed at high temperature (Figure 7b, Figure S3). The magnitude of the change in the intensity of feature C varied with composition. The change in the intensity of feature C appears to correspond with changes in the lattice parameters determined by XRD (Table 1, Figure 3), and a change in the intensity of feature C was observed when a change in the lattice constant was observed. The intensity of feature C in the spectrum from the $Nd_{0.25}Zr_{0.75}O_{1.88}$ sample annealed at 1400 °C was more intense than the intensity of feature C the spectrum from the $Nd_{0.25}Zr_{0.75}O_{1.88}$ sample annealed at 1500 °C. The increase in the intensity of feature C could be attributed to increased ordering within the system, and these results likely indicate that the local ordering was slightly greater in $Nd_{0.25}Zr_{0.75}O_{1.88}$ annealed at 1400 °C than in $Nd_{0.25}Zr_{0.75}O_{1.88}$ annealed at 1500 °C. These observations could explain the origin of the changes in the lattice constants of the $Nd_xY_{0.25-x}O_{1.88}$ materials made by co-precipitation upon annealing.

The spectra were fitted to determine the scattering path lengths and ordering parameters, and these results are enumerated in Table 2 and Table S1. The calculated fits and data are compared in Figures 7c,d and Figures S5-S10. In all cases, the Zr–O scattering path length was found to be 2.16 Å, which is consistent with previously reported results.[24,27,36,60] The Zr–Zr/Y scattering path length was 3.56 Å, which is also in agreement with previously reported results.[24,27,36,60] The Zr–Nd path lengths determined from the EXAFS fit varied from 3.18 Å – 3.77 Å, depending on composition and annealing temperature. The most significant change occurred when the $Nd_{0.25}Zr_{0.75}O_{1.88}$ material made by co-precipitation was annealed at both 1400 °C and 1500 °C, as the Zr–Nd scattering path decreased from 3.77 Å to 3.36 Å (Table S1). The Zr–Nd scattering path length also changed when the $Nd_{0.05}Y_{0.20}Zr_{0.75}O_{1.88}$ material synthesized via the co-precipitation route was annealed (Table S1). Here, the path length decreased from 3.70 Å to 3.44 Å upon annealing at 1400 °C. The Zr–Nd scattering path

length did not change when the other $Nd_xY_{0.25x}Zr_{1-x-y}O_{1.88}$ materials were annealed at high temperature, and was consistently low, with values under 3.4 Å. These values are unphysical given the fluorite lattice, and it has been previously hypothesized by our group that these values *possibly* indicate that a Zr- and Y-doped B-Nd_2O_3 type structure, which has a 3.428 Å M–M bond length, is present in the material.[39,61] Failures in the fitting model must also be considered as a source of these abnormally low values as well, though these possible failures would not affect the fitted parameters of the Zr–Zr/Y and Zr–O scattering paths.

The Fourier-transformed EXAFS spectra from the as-synthesized and annealed $Nd_xY_{0.25-x}Zr_{0.75}O_{1.88}$ materials made by the co-precipitation method are compared to the EXAFS spectra from the materials made by the ceramic method in Figures 8 and S4. The intensities of peaks C and D in the spectra from the as-synthesized materials made by co-precipitation are less than the intensities of peaks C and D in the spectra from the materials made by the ceramic method and the materials made by the co-precipitation method annealed at 1500 °C. The increase in the intensities of these features may be explained by increased ordering within the materials made by the ceramic method and the materials annealed at 1500 °C compared to the as-synthesized materials made by the co-precipitation method. This is consistent with the lower synthetic temperature of the co-precipitation method, and also agrees with powder XRD results. The spectra from the materials made by the ceramic method and the materials made by the co-precipitation method annealed at 1500 °C are similar. This indicates that the the local structure around the Zr metal centres are similar, and that the local Zr structure is more dependent on annealing/synthetic temperature and less on the synthetic method.

3.4. Y K-edge XAS

3.4.1. XANES

Y K-edge XANES spectra were collected from several of the as-synthesized and high-temperature annealed $Nd_xY_{1-x}Zr_{0.75}O_{1.88}$ materials made by the co-precipitation method, and these spectra are presented in Figure 9 and Figure S11. Three features were observed in the Y K-edge spectra, labelled as E, F, and F' in Figure 9a. Similar to the Zr K-edge, feature E arises from forbidden, quadrapolar Y 1s → 4d transitions and features F and F' are due to dipolar Y 1s → 5p transitions.[36] The spectra did not change when the composition was varied.

This indicates that the Y coordination environment does not depend on the composition of materials made via the co-precipitation route.

The spectra from the as-synthesized materials and materials annealed at high temperatures made via co-precipitation are presented in Figure 9b. As with changes in composition, no significant changes in the spectra were observed when the $Nd_xY_{1-x}Zr_{0.75}O_{1.88}$ materials were annealed at high temperatures. This suggests that the majority of the changes that occur when the materials are annealed at high temperature are located around either the Zr or Nd metal centres. Further, only minor differences between XANES spectra from materials made by the co-precipitation and the ceramic synthetic methods were observed (Figure 9c, Figure S11). This indicates that the Y coordination environment was not affected by the synthetic method used. Overall, the Y K-edge XANES results indicate that the Y coordination environment was stable when the $Nd_xY_{0.25-x}Zr_{0.75}O_{1.88}$ materials made by a co-precipitation synthesis were annealed at high temperature.

3.4.2. EXAFS

Y K-edge EXAFS spectra were collected from the as-synthesized $Nd_xY_{1-x}Zr_{0.75}O_{1.88}$ materials as well as materials made by co-precipitation that were annealed at high temperature. The Fourier transformed EXAFS spectra from the as-synthesized materials are presented in Figure 10. Two features were observed, and these features are labelled as G and H in Figure 10a. Feature G arises from the first shell Y–O scattering path and feature H is assigned to second shell Y–Y, Y–Zr, and Y–Nd scattering paths.[27,36] Only minor variations in the intensities of features G and H were observed as the composition of the $Nd_xY_{1-x}Zr_{0.75}O_{1.88}$ materials was varied. This is in contrast to the previous study of $Nd_xY_{1-x}Zr_{0.75}O_{1.88}$ materials made by the ceramic method, in which the intensity of feature H decreased with increased Nd content.[39] In this previous study, the change in the intensity of feature H was attributed to interference between the Y–Nd and Y–Y/Zr scattering paths.[39] A similar trend was not observed in the spectra from materials made by the co-precipitation route. This could be due to non-homogenous distribution of Nd and Y in the materials made by co-precipitation, with Nd preferentially occupying sites that are separated from Y in these materials. Here, the materials were likely heterogeneous on a short-range to intermediate scale, and this heterogeneity may not be observed in the WDS results.

The intensity of feature H increased when the $Nd_xY_{1-x}Zr_{0.75}O_{1.88}$ materials made by co-precipitation were annealed at high temperature while only small changes in the intensity of feature G were observed (Figure 10b,

Figure S12). The increase in intensity of feature H can be explained by the increased long-range ordering in the system, as was shown by the analysis of the powder XRD patterns. In contrast, no changes in the EXAFS spectra were observed when the $Nd_xY_{1-x}Zr_{0.75}O_{1.88}$ materials made by the ceramic method were annealed at high temperature.[39] This is because the materials made via ceramic reaction were already highly crystalline, and the long-range ordering did not increase appreciably upon annealing.

The EXAFS spectra from the as-synthesized and annealed $Nd_xY_{0.25-x}Zr_{0.75}O_{1.88}$ materials made by the co-precipitation method were modelled to determine the scattering path lengths and disorder parameters of the Y–O, Y–Y/Zr, and Y–Nd scattering paths, and the results of these fits are presented in Table 3 and Table S2, and the fitted spectra are plotted in Figures 10c and 10d, and Figures S13-S16. The Y–O scattering path length was determined to be 2.32 Å, which is in agreement with previously reported values.[27,36,60,62] The Y–O scattering path lengths and σ^2 values did not change when the composition was varied or when the materials were annealed at high temperature, which is consistent with the Y K-edge XANES results. The Y–Y/Zr scattering path length and σ^2 also did not vary significantly when the composition was varied or when the materials were annealed at high temperature, and the average scattering path length was 3.65 Å. This value is in agreement with previously reported results.[39] The Y–Nd scattering path value was found to be 3.39-3.40 Å in all materials except for the $Nd_{0.15}Y_{0.10}Zr_{0.75}O_{1.88}$ sample annealed at 1500 °C, where the Y–Nd scattering path was determined to be 3.62 Å (Table 3, Table S2). The lower values are not physically meaningful in a fluorite structure, and it has been previously postulated that these results *may* indicate that a Zr- and Y-doped c-Nd_2O_3 type structure is present in the material in which Y is intimately mixed with Nd.[39] The σ^2 values of the Y–Nd scattering path were also fitted to unrealistically small value in all cases. The Y–Y/Zr and Y–Nd CNs had to be varied to ensure fit a value of $\sigma^2_{Y\text{-}Nd} > 0$ in the case of the $Nd_{0.15}Y_{0.10}Zr_{0.75}O_{1.88}$ and $Nd_{0.20}Y_{0.05}Zr_{0.75}O_{1.88}$ materials prepared by co-precipitation and annealed at 1400 °C. This suggests that the model did not adequately account for the Y–Nd contributions, though the scattering path lengths and σ^2 values of the Y–Y and Y–O scattering pathways likely remain valid.

The Fourier-transformed Y K-edge EXAFS spectra from $Nd_xY_{1-x}Zr_{0.75}O_{1.88}$ materials made via the co-precipitation and ceramic synthetic method are compared in Figure 11 and Figure S12. The intensities of features G and H are suppressed in the spectrum from the as-synthesized $Y_{0.25}Zr_{0.75}O_{1.88}$ material made by the co-precipitation method compared to the same material made by the ceramic route. This can be explained by a lower

degree of ordering in the co-precipitated material and is consistent with the powder XRD results. However, the spectrum from the co-precipitated $Y_{0.25}Zr_{0.75}O_{1.88}$ material annealed at 1500 °C is identical to the spectrum from the $Y_{0.25}Zr_{0.75}O_{1.88}$ material made by the ceramic method at 1500 °C, which indicates that the Y coordination environment is identical in this case (Figure 11a). A similar result was observed for other $Nd_xY_{1-x}Zr_{0.75}O_{1.88}$ materials studied here with the exception of $Nd_{0.20}Y_{0.05}Zr_{0.75}O_{1.88}$. In this case, feature H in the spectrum from $Nd_{0.20}Y_{0.05}Zr_{0.75}O_{1.88}$ made by the ceramic method was less intense than feature H in the spectra from the as-synthesized $Nd_{0.20}Y_{0.05}Zr_{0.75}O_{1.88}$ and $Nd_{0.20}Y_{0.05}Zr_{0.75}O_{1.88}$ annealed at 1500 °C made by the co-precipitation route (Figure 11b). This could indicate that Nd occupied more sites further from the Y metal centres in these materials made by the co-precipitation route as destructive interference between the Y–Y/Zr and Y–Nd scattering paths would lead to a decrease in the intensity of feature H. The Y K-edge EXAFS results indicate that using a co-precipitation synthesis with a low calcining temperature (800 °C) results in increased local disorder in the $Nd_xY_{1-x}Zr_{0.75}O_{1.88}$ materials compared to the ceramic synthesis, which is performed at high temperature (1500 °C). The increased disorder in the as-synthesized materials made by the co-precipitation method is due to the lower synthetic temperature, and when these "as-synthesized" materials are annealed at high temperature (i.e., 1500 °C) the local and intermediate Y ordering becomes nearly identical to that of the materials made by the ceramic method.

4. Conclusions

The thermal stability, long-range structure, and local structure in a series of $Nd_xY_{0.25-x}Zr_{0.75}O_{1.88}$ materials made by a co-precipitation method have been characterized and compared to $Nd_xY_{0.25-x}Zr_{0.75}O_{1.88}$ materials made by a ceramic route.[39] This study has shown that $Nd_xY_{0.25-x}Zr_{0.75}O_{1.88}$ materials can be successfully synthesized at low temperatures using the co-precipitation route. However, these materials are less crystalline and are more disordered than materials made by the ceramic synthetic route. Further, the compositional range at which the fluorite structure is stable at high temperatures is also diminished. The $Nd_xY_{0.25-x}Zr_{0.75}O_{1.88}$ materials made by the co-precipitation method were only stable at 1400 °C when $x \leq 0.15$, whereas the fluorite structure for materials made by the ceramic method was stable when $x \leq 0.20$. The materials made by the co-precipitation method are more kinetically labile due to the intimate mixing of the component cations on an atomic level.[51–53,63]

The XAS results showed that the local coordination environments around the Zr and Y cations were largely similar in the materials made by the co-precipitation method and the ceramic method. The Y K-edge EXAFS and XANES spectra from the compounds made by co-precipitation and those made by ceramic synthesis were identical when the co-precipitated materials were annealed at 1500 °C, with the exception of $Nd_{0.20}Y_{0.05}Zr_{0.75}O_{1.88}$. These results generally indicate that the main source of long-range disorder within the materials made by the co-precipitation route came from differences in the arrangements of the metal-oxygen polyhedra rather than from disorder within the metal-oxygen polyhedra. The intermediate and long-range structure is strongly dependent on annealing temperature, and the structure becomes more ordered with increased annealing temperature. Overall, this study concludes that $Nd_xY_{0.25-x}Zr_{0.75}O_{1.88}$ compounds with $x \leq 0.15$ made by a co-precipitation method could be suitable IMF candidates. The reduced annealing times required to produce these materials could lead to a significant opportunity to reduce the cost of producing IMF fuels.

Acknowledgements

The Natural Sciences and Engineering Research Council (NSERC) of Canada supported this work through a discovery grant awarded to APG. JRH would also like to thank NSERC for financial support through the Canada Graduate Scholarship program and the University of Saskatchewan. The Canadian Foundation for Innovation (CFI) is thanked for providing funds to purchase the PANalytical Empyrean powder X-ray diffractometer used in this work. The authors extend their thanks to Dr. Zou Finfrock and Dr. Robert Gordon for their help in carrying out XAS measurements at 20BM (CLS@APS Sector 20, APS). In addition, Mr. M. R. Ruffadin and Ms. E.R. Aluri (Department of Chemistry, University of Saskatchewan) are thanked for helping with the collection of the XANES spectra presented in this study. The authors would like to thank Dr. R. Ham-Su, Dr. L. Dickson, and Dr. M. Saoudi of the Canadian Nuclear Laboratories Limited (CNL) for their support of this work. Mr. B. Novakovski and Mr. T. Bonli (University of Saskatchewan) are thanked for their help in the sample preparation for SEM analysis and for collecting the SEM images and WDS measurements. Access to Sector 20 was obtained through the CLS-APS Partnership Agreement. Sector 20 facilities at the Advanced Photon Source, and research at these facilities, are supported by the US Department of Energy - Basic Energy Sciences, the Canadian Light Source and its funding partners, the University of Washington, and the Advanced Photon Source.

Use of the Advanced Photon Source, an Office of Science User Facility operated for the U.S. Department of Energy (DOE) Office of Science by Argonne National Laboratory, was supported by the U.S. DOE under Contract No. DE-AC02-06CH11357. The CLS is supported by NSERC, the National Research Council of Canada, the Canadian Institutes of Health Research, the Province of Saskatchewan, Western Economic Diversification Canada, and the University of Saskatchewan.

References

(1) Kharecha, P. A.; Hansen, J. E. *Environ. Sci. Technol.* **2013**, *47* (9), 4889–4895.

(2) Hoffert, M. I.; Caldeira, K.; Benford, G.; Criswell, D. R.; Green, C.; Herzog, H.; Jain, A. K.; Kheshgi, H. S.; Lackner, K. S.; Lewis, J. S.; Lightfoot, H. D.; Manheimer, W.; Mankins, J. C.; Mauel, M. E.; Perkins, L. J.; Schlesinger, M. E.; Volk, T.; Wigley, T. M. L. *Science* **2002**, *298* (5595), 981–987.

(3) Hoffert, M. I.; Caldeira, K.; Jain, a. K.; Haites, E. F.; Harvey, L. D. D.; Potter, S. D.; Schlesinger, M. E.; Schneider, S. H.; Watts, R. G.; Wigley, T. M. L.; Wuebbles, D. J. *Nature* **1998**, *395* (October), 881–884.

(4) Lenzen, M. *Energy Convers. Manag.* **2008**, *49* (8), 2178–2199.

(5) Chapman, N.; Hooper, A. *Proc. Geol. Assoc.* **2012**, *123* (1), 46–63.

(6) Rempe, N. T. *Prog. Nucl. Energy* **2007**, *49* (5), 365–374.

(7) Lombardi, C.; Luzzi, L.; Padovani, E.; Vettraino, F. *Prog. Nucl. Energy* **2008**, *50* (8), 944–953.

(8) Salvatores, M. *Nucl. Eng. Des.* **2005**, *235* (7), 805–816.

(9) Prítrský, J.; Nečas, V. *Prog. Nucl. Energy* **2012**, *54* (1), 36–40.

(10) Degueldre, C.; Paratte, J. M. *J. Nucl. Mater.* **1999**, *274* (1-2), 1–6.

(11) Ledergerber, G.; Degueldre, C.; Heimgartner, P.; Pouchon, M. A.; Kasemeyer, U. *Prog. Nucl. Energy* **2001**, *38* (3-4), 301–308.

(12) Lombardi, C.; Mazzola, A. *Ann. Nucl. Energy* **1996**, *23* (14), 1117–1126.

(13) Holliday, K.; Hartmann, T.; Poineau, F.; Rory Kennedy, J.; Czerwinski, K. *J. Nucl. Mater.* **2009**, *393* (2), 224–229.

(14) Kamel, N.; Aït-Amar, H.; Taouinet, M.; Benazzouz, C.; Kamel, Z.; Fodil-Cherif, H.; Telmoune, S.; Slimani, R.; Zahri, A.; Sahel, D. *Prog. Nucl. Energy* **2006**, *48* (1), 70–84.

(15) Degueldre, C. *J. Alloys Compd.* **2007**, *444-445*, 36–41.

(16) Pouchon, M. A.; Degueldre, C.; Tissot, P. *Thermochim. Acta* **1998**, *323* (1-2), 109–121.

(17) Pöml, P.; Konings, R. J. M.; Somers, J.; Wiss, T.; de Haas, G. J. L. M.; Klaassen, F. C. In *Comprehensive Nuclear Materials Volume 3*; Konings, R. J. M., Allen, T. R., Stoller, R. E., Yamanaka, S., Eds.; Elsevier, 2012; pp 237–256.

(18) Lumpkin, G. R. *Elements* **2006**, *2*, 365–372.

(19) Shibata, N.; Katamura, J.; Kuwabara, A.; Ikuhara, Y.; Sakuma, T. *Mater. Sci. Eng. A* **2001**, *312* (1-2), 90–98.

(20) Guo, X. *Phys. Status Solidi* **2000**, *177* (1), 191–201.

(21) Lemonnier, S.; Grandjean, S.; Robisson, A.-C.; Jolivet, J.-P. *Dalton Trans.* **2010**, *39* (9), 2254–2262.

(22) Kinoshita, H.; Kuramoto, K.; Uno, M.; Yanagi, T.; Yamanaka, S.; Mitamura, H.; Banba, T. *J. Am. Ceram. Soc.* **2000**, *83*, 391–396.

(23) Li, P.; Chen, I.; Penner-Hahn, J. E. *Phys. Rev. B* **1993**, *48* (14), 63–73.

(24) Belin, R. C.; Martin, P. M.; Valenza, P. J.; Scheinost, A. C. *Inorg. Chem.* **2009**, *48* (12), 5376–5381.

(25) Xu, G.; Ming, W.; Yao, Y.; Dai, X.; Zhang, S.-C.; Fang, Z. *Eur. Lett.* **2008**, *82* (6), 67002.

(26) Zhang, F.; Chupas, P. J.; Lui, S. L. A.; Hanson, J. C.; Caliebe, W. A.; Lee, P. L.; Chan, S.-W. *Chem. Mater.* **2007**, *19* (13), 3118–3126.

(27) Catlow, C. R. A.; Chadwick, A. V; Greaves, G. N.; Moroney, L. M. *J. Am. Ceram. Soc.* **1986**, *69* (3), 272–277.

(28) Degueldre, C.; Pouchon, M.; Döbeli, M.; Sickafus, K.; Hojou, K.; Ledergerber, G.; Abolhassani-Dadras, S. *J. Nucl. Mater.* **2001**, *289* (1-2), 115–121.

(29) Van Hassel, B. A.; Burggraaf, A. J. *Appl. Phys. A* **1991**, *53*, 155–163.

(30) Bekale, V. M.; Huntz, a. M.; Legros, C.; Sattonnay, G.; Jomard, F. *Philos. Mag.* **2008**, *88* (1), 1–19.

(31) Zavodinsky, V. G.; Chibisov, A. N. *Phys. Solid State* **2006**, *48* (2), 363–368.

(32) Degueldre, C.; Arima, T.; Lee, Y. W. *J. Nucl. Mater.* **2003**, *319*, 6–14.

(33) Villella, P.; Conradson, S.; Espinosa-Faller, F.; Foltyn, S.; Sickafus, K.; Valdez, J.; Degueldre, C. *Phys. Rev. B* **2001**, *64* (10), 104101.

(34) Lanteri, V.; Heuer, A. H.; Mitchell, T. E. In *Science and Technology of Zirconia II*; Hobbs, L. W., Ed.; The American Ceramic Society, 1985; Vol. 12, pp 118–130.

(35) Fabrichnaya, O.; Savinykh, G.; Schreiber, G.; Seifert, H. J. *J. Phase Equilibria Diffus.* **2011**, *32* (4), 284–297.

(36) Li, P.; Chen, I.-W.; Penner-Hahn, J. E. *Phys. Rev. B* **1993**, *48* (14), 10074–10081.

(37) Bocanegra-Bernal, M. H.; Díaz de la Torre, S. *J. Mater. Sci.* **2002**, *37*, 4947–4971.

(38) Ronchi, C.; Ottaviani, J. P.; Degueldre, C.; Calabrese, R. *J. Nucl. Mater.* **2003**, *320* (1-2), 54–65.

(39) Hayes, J. R.; Grosvenor, A. P.; Saoudi, M. *J. Alloys Compd.* **2015**, *635*, 245–255.

(40) Vaidya, V. N. *J. Sol-Gel Sci. Technol.* **2008**, *46* (3), 369–381.

(41) Arachi, Y. *Solid State Ionics* **2004**, *175* (1-4), 119–121.

(42) PANalytical HighScore Plus Version 3.0.4 (2011) PANaltyical BV: Amelo, The Netherlands.

(43) Igawa, N.; Ishii, Y. *J. Am. Ceram. Soc.* **2001**, *84* (5), 1169–1171.

(44) Bondars, B.; Heidemane, G.; Grabis, J.; Laschke, K.; Boysen, H.; Schneider, J.; Frey, F. *J. Mater. Sci.* **1995**, *30* (6), 1621–1625.

(45) Jaffe, J.; Bachorz, R.; Gutowski, M. *Phys. Rev. B* **2005**, *72* (14), 144107.

(46) Heald, S. M.; Brewe, D. L.; Stern, E. A.; Kim, K. H.; Brown, F. C.; Jiang, D. T.; Crozier, E. D.; Gordon, R. A. *J. Synchrotron Rad.* **1999**, *6* (Pt 3), 347–349.

(47) Thompson, A.; Attwood, D.; Gullikson, E.; Howells, M.; Kim, K.-J.; Kirz, J.; Kortright, J.; Lindau, I.; Pianetta, P.; Robinson, A.; Scofield, J.; Underwood, J.; Vaughn, D.; Williams, G.; Winick, H. *X-ray Data Booklet*; Lawrence Berkeley National Laboratory: Berkeley, 2009.

(48) Newville, M. *Fundamentals of XAFS*, 1.7 ed.; University of Chicago: Chicago, 2004.

(49) Rehr, J.; Albers, R. *Phys. Rev. B* **1990**, *41* (12), 8139–8149.

(50) Ravel, B.; Newville, M. *J. Synchrotron Rad.* **2005**, *12* (Pt 4), 537–541.

(51) Suárez, G.; Garrido, L. B.; Aglietti, E. F. *Mater. Chem. Phys.* **2008**, *110* (2-3), 370–375.

(52) Song, X.; Lu, J.; Zhang, T.; Ma, J. *J. Am. Ceram. Soc.* **2011**, *94* (4), 1053–1059.

(53) Fujimori, H.; Yashima, M.; Kakihana, M.; Yoshimura, M. *J. Am. Ceram. Soc.* **1998**, *81* (11), 2885–2893.

(54) Schelling, P. K.; Phillpot, S. R.; Wolf, D. *J. Am. Ceram. Soc.* **2001**, *84* (7), 1609–1619.

(55) Denton, A.; Ashcroft, N. *Phys. Rev. A* **1991**, *43* (6), 3161–3164.

(56) Walker, J. D. S.; Grosvenor, A. P. *Inorg. Chem.* **2013**, *52* (15), 8612–8620.

(57) Hayes, J. R.; Grosvenor, A. P.; Sao. *Unpublished*.

(58) Mountjoy, G.; Pickup, D. M.; Anderson, R.; Wallidge, G. W.; Holland, M. A.; Newport, R. J.; Smith, M. E. *Phys. Chem. Chem. Phys.* **2000**, *2* (10), 2455–2460.

(59) Mountjoy, G.; Holland, M. A.; Wallidge, G. W.; Gunawidjaja, P.; Smith, M. E.; Pickup, D. M.; Newport, R. J. *J. Phys. Chem. B* **2003**, *107* (31), 7557–7566.

(60) Gómez, A.; Villanueva, R.; Vie, D.; Murcia-Mascaros, S.; Martínez, E.; Beltrán, A.; Sapiña, F.; Vicent, M.; Sánchez, E. *J. Solid State Chem.* **2013**, *197*, 120–127.

(61) Wu, B.; Zinkevich, M.; Aldinger, F.; Wen, D.; Chen, L. *J. Solid State Chem.* **2007**, *180* (11), 3280–3287.

(62) Walter, M.; Nästren, C.; Somers, J.; Jardin, R.; Denecke, M. A.; Brendebach, B. *J. Solid State Chem.* **2007**, *180* (11), 3130–3135.

(63) Schelling, P. K.; Phillpot, S. R.; Wolf, D. *J. Am. Ceram. Soc.* **2001**, *84* (7), 1609–1619.

Tables

Table 1: Summary of Rietveld Refinement Results

	$Y_{0.25}Zr_{0.75}O_{1.88}$			$Nd_{0.05}Y_{0.20}Zr_{0.75}O_{1.88}$		
	As synth	**An. 1400 °C**	**An. 1500 °C**	**As synth**	**An. 1400 °C**	**An. 1500 °C**
Rwp	7.32	8.62	8.54	7.28	9.61	9.03
Unit Cell	5.1489(5)	5.15163(5)	5.15113(6)	5.1534(4)	5.15553(5)	5.15675(5)
Wt. Fraction	100% Cubic	100% Cubic	100% Cubic	100% Cubic	100% Cubic	100% Cubic
	$Nd_{0.10}Y_{0.15}Zr_{0.75}O_{1.88}$			$Nd_{0.15}Y_{0.10}Zr_{0.75}O_{1.88}$		
	As synth	**An. 1400 °C**	**An. 1500 °C**	**As synth**	**An. 1400 °C**	**An. 1500 °C**
Rwp	7.12	8.74	8.01	7.50	8.85	8.94
Unit Cell	5.1596(4)	5.16052(6)	5.16101(6)	5.1715(4)	5.17165(6)	5.17329(6)
Wt. Fraction	100% Cubic	100% Cubic	100% Cubic	100% Cubic	100% Cubic	100% Cubic
	$Nd_{0.20}Y_{0.05}Zr_{0.75}O_{1.88}$			$Nd_{0.25}Zr_{0.75}O_{1.88}$		
	As synth	**An. 1400 °C**	**An. 1500 °C**	**As synth**	**An. 1400 °C**	**An. 1500 °C**
Rwp	9.27	9.03	N/A	7.90	7.29	7.10
Unit Cell	5.1763(4)	5.18281(7)	5.17924(6)	5.1852(3)	5.2065(1)	5.19341(6)
Wt. Fraction	100% Cubic	92.6% Cubic 4.0% Tetragonal 3.4% Monoclinic	Unknown Phases Present	100% Cubic	71.7% Cubic 3.6% Tetragonal 24.7% Monoclinic	85.5% Cubic 14.5% Monoclinic

Table 2: Zr K-edge EXAFS Fit Results

	$Nd_{0.15}Y_{0.10}Zr_{0.75}O_{1.88}$								
	As-synthesized $S_o^2 = 0.90(6)$, $\Delta E = -3.9(7)$ eV $R_{fit} = 0.0165$			Annealed 1400 °C $S_o^2 = 0.78(6)$, $\Delta E = -4.0(7)$ eV $R_{fit} = 0.0165$			Annealed 1500 °C $S_o^2 = 0.92(7)$, $\Delta E = -3.9(8)$ eV $R_{fit} = 0.0199$		
	CN	R (Å)	σ^2	CN	R (Å)	σ^2	CN	R (Å)	σ^2
Zr–O	7	2.16(1)	0.008(1)	8	2.160(8)	0.007(1)	7	2.160(8)	0.008(1)
Zr–Zr/Y	10.2	3.56(1)	0.011(1)	10.2	3.56(1)	0.009(1)	10.2	3.56(1)	0.010(1)
Zr–Nd	1.8	3.21(4)	0.013(6)	1.8	3.19(4)	0.011(6)	1.8	3.19(4)	0.011(5)
Zr–O2	24	4.36(4)	0.04(1)	24	4.33(4)	0.027(8)	24	4.35(4)	0.04(1)
	$Nd_{0.20}Y_{0.05}Zr_{0.75}O_{1.88}$								
	As-synthesized $S_o^2 = 0.82(8)$, $\Delta E = -3.8(9)$ eV $R_{fit} = 0.0259$			Annealed 1400 °C $S_o^2 = 0.82(8)$, $\Delta E = -3.6(9)$ eV $R_{fit} = 0.0314$			Annealed 1500 °C $S_o^2 = 0.85(8)$, $\Delta E = -4(1)$ eV $R_{fit} = 0.0323$		
	CN	R (Å)	σ^2	CN	R (Å)	σ^2	CN	R (Å)	σ^2
Zr–O	7	2.16(1)	0.007(1)	7	2.16(1)	0.007(2)	7	2.16(2)	0.007(2)
Zr–Zr/Y	9.6	3.58(1)	0.011(1)	9.6	3.57(1)	0.011(1)	9.6	3.57(1)	0.011(1)
Zr–Nd	2.4	3.36(1)	0.04(5)	2.4	3.36(1)	0.04(4)	2.4	3.36(3)	0.07(2)
Zr–O2	24	4.34(6)	0.03(1)	24	4.36(5)	0.03(1)	24	4.35(6)	0.03(1)

Table 3 Y K-edge EXAFS Fit Results

	$Nd_{0.15}Y_{0.10}Zr_{0.75}O_{1.88}$								
	As-synthesized S_o^2 = 0.8(1), ΔE = -4(1) eV R_{fit} = 0.024			Annealed 1400 °C S_o^2 = 0.8(1), ΔE = -4(1) eV R_{fit} = 0.023			Annealed 1500 °C S_o^2 = 0.8(1), ΔE = -3(1) eV R_{fit} = 0.039		
	CN	R (Å)	σ^2	CN	R (Å)	σ^2	CN	R (Å)	σ^2
Y–O	8	2.32(1)	0.009(2)	8	2.32(1)	0.008(2)	8	2.33(2)	0.007(3)
Y–Zr/Y	10.2	3.65(1)	0.007(2)	10	3.66(1)	0.006(2)	10.2	3.63(2)	0.004(2)
Y–Nd	1.8	3.40(3)	0.003(3)	2	3.40(3)	0.002(3)	1.8	3.62(3)	0.000(4)
Y–O2	24	4.7(2)	0.06(4)	24	4.7(3)	0.08(6)	24	4.50(7)	0.03(2)
	$Nd_{0.20}Y_{0.05}Zr_{0.75}O_{1.88}$								
	As-synthesized S_o^2 = 0.8(1), ΔE = -4(1) eV R_{fit} = 0.028			Annealed 1400 °C S_o^2 = 0.8(1), ΔE = -4(1) eV R_{fit} = 0.020			Annealed 1500 °C S_o^2 = 0.8(1), ΔE = -4(1) eV R_{fit} = 0.025		
	CN	R (Å)	σ^2	CN	R (Å)	σ^2	CN	R (Å)	σ^2
Y–O	8	2.33(2)	0.008(2)	8	2.32(1)	0.008(2)	8	2.32(1)	0.007(2)
Y–Zr/Y	9.6	3.66(2)	0.007(2)	10	3.65(1)	0.007(2)	9.6	3.66(1)	0.006(2)
Y–Nd	2.4	3.40(4)	0.005(4)	2	3.40(3)	0.003(3)	2.4	3.40(3)	0.003(3)
Y–O2	24	4.7(2)	0.07(5)	24	4.7(2)	0.07(5)	24	4.8(3)	0.08(7)

Figure Captions

Figure 1: Powder X-ray diffraction patterns from the as-synthesized and annealed (a) $Nd_{0.20}Y_{0.05}Zr_{0.75}O_{1.88}$ and (b) $Y_{0.25}Zr_{0.75}O_{1.88}$ materials made by the co-precipitation method. The as synthesized samples are denoted as "As synth." and the annealed samples are denoted as "An." in all figures. A small amount of monoclinic and tetragonal ZrO_2 phase was formed when the $Nd_{0.20}Y_{0.05}Zr_{0.75}O_{1.88}$ material was annealed at 1400 °C and an unidentified phase was produced when the material was annealed at 1500 °C, which is not included in the fit. The $Y_{0.25}Zr_{0.75}O_{1.88}$ material maintained a single fluorite phase when annealed at 1400 °C and 1500 °C.

Figure 2: Powder X-ray diffraction patterns of $Nd_{0.25}Zr_{0.75}O_{1.88}$ prepared by (a) co-precipitation and (b) ceramic synthetic routes.[39] Monoclinic and tetragonal zirconia phases were formed when the materials prepared by both synthetic routes were annealed at 1400 °C. A monoclinic zirconia phase was observed when the material prepared by the co-precipitation method was annealed at 1500 °C. No monoclinic zirconia phase was observed in the as-synthesized material made by the ceramic synthetic route (which was fired at 1500 °C).

Figure 3: The lattice parameters of the as-synthesized and annealed $Nd_xY_{0.25-x}Zr_{0.75}O_{1.88}$ materials made via the co-precipitation route are plotted as function of Nd content. The lattice parameters of the $Nd_xY_{0.25-x}Zr_{0.75}O_{1.88}$ materials made by the ceramic synthetic route at 1500 °C are also included. The black dashed lines are the linear best fit line of the as-synthesized materials made by the co-precipitation and ceramic route, and indicate that Vegard's law is followed in both cases.

Figure 4: Micrographs collected from as-synthesized $Y_{0.25}Zr_{0.75}O_{1.88}$ and $Y_{0.25}Zr_{0.75}O_{1.88}$ annealed at 1400 °C prepared by a co-precipitation method are presented. (a) A BSE image from the as-synthesized $Y_{0.25}Zr_{0.75}O_{1.88}$ and (b) the Y L_α WDS map from the same spot. (c) A BSE image from the $Y_{0.25}Zr_{0.75}O_{1.88}$ annealed at 1400 °C and (d) the Y L_α WDS map from the same spot. All images were collected at the same magnification and a scale bar is shown in (a).

Figure 5: Micrographs collected from as-synthesized $Nd_{0.20}Y_{0.05}Zr_{0.75}O_{1.88}$ and $Nd_{0.20}Y_{0.05}Zr_{0.75}O_{1.88}$ annealed at 1400 °C prepared by a co-precipitation method are presented. (a) A BSE image from the as-synthesized $Nd_{0.20}Y_{0.05}Zr_{0.75}O_{1.88}$, (b) the Nd L_α WDS map, (c) the Y L_α WDS map from the same spot. (d) A BSE image from the $Nd_{0.20}Y_{0.05}Zr_{0.75}O_{1.88}$ annealed at 1400 °C and (e) the Nd L_α WDS map, and (f) the Y L_α WDS map from the same spot. All images were collected at the same magnification and a scale bar is shown in (a).

Figure 6: (a) The Zr K-edge XANES spectra from the as-synthesized $Nd_xY_yZr_{1-x-y}O_{2-\delta}$ materials prepared by co-precipitation are compared. Three features, labelled A, B, and B' were observed. Feature A is attributed to 1s → 4d transitions and features B and B' are attributed to 1s → 5p transitions. (b) The XANES spectra from the as-synthesized and annealed materials prepared by co-precipitation are compared. Changes in the spectra were only observed when the $Nd_{0.25}Zr_{0.75}O_{1.88}$ materials were annealed. *Inset*: An expanded view of the XANES spectra from the $Nd_{0.25}Zr_{0.75}O_{1.88}$ materials showing the changes that occurred upon annealing. (c) The spectra from the $Nd_xY_yZr_{1-x-y}O_{2-\delta}$ materials made at 800 °C via a co-precipitation method and made at 1500 °C via a ceramic method are compared. Also included are spectra from the materials made by co-precipitation annealed at 1500 °C.

Figure 7: (a) The Fourier-transformed Zr K-edge EXAFS spectra from the as-synthesized $Nd_xY_yZr_{1-x-y}O_{2-\delta}$ materials prepared by co-precipitation are presented. Feature C is attributed to first shell Zr–O scattering paths and feature D is attributed to second shell Zr–Zr, Zr–Y, and Zr–Nd scattering paths. (b) The Fourier-transformed EXAFS spectra from the as-synthesized and annealed $Nd_{0.25}Zr_{0.75}O_{1.88}$ spectra are presented. The intensities of features C and D increase with increased annealing temperature. The fitted spectrum from $Nd_{0.15}Y_{0.10}Zr_{0.75}O_{1.88}$ is compared to the data in (c) R-space and (d) k-space.

Figure 8: The Fourier-transformed Zr K-edge EXAFS spectra from the (a) $Nd_{0.25}Zr_{0.75}O_{1.88}$ and (b) $Nd_{0.20}Y_{0.05}Zr_{0.75}O_{1.88}$ materials prepared by co-precipitation and ceramic synthetic methods are compared. Also included is the material made via co-precipitation annealed at 1500 °C. Features C and D are more intense in the spectra from the materials made via the ceramic synthetic route as compared to both materials made via the co-precipitation route, indicating increased local ordering around the Zr metal centres.

Figure 9: (a) Y K-edge XANES spectra from the as-synthesized $Nd_xY_yZr_{1-x-y}O_{2-\delta}$ materials synthesized by co-precipitation are presented. Three features were observed, labelled E, F, and F'. Feature E arises due to 1s → 4d transitions and feature F and F' arise from 1s → 5p transitions. (b) The Y K-edge spectra from the as-synthesized and annealed $Nd_xY_yZr_{1-x-y}O_{2-\delta}$ materials are presented. No significant changes were observed when the materials were annealed at 1400 °C and 1500 °C. (c) The spectra from $Nd_{0.20}Y_{0.05}Zr_{0.75}O_{1.88}$ materials made via co-precipitation and ceramic synthetic routes are compared. No significant changes are observed in the spectra from the materials made using different synthetic routes.

Figure 10: (a) The Fourier-transformed Y K-edge EXAFS spectra from the as-synthesized $Nd_xY_yZr_{1-x-y}O_{2-\delta}$ materials synthesized by co-precipitation are presented are shown. First shell Y–O scattering paths contribute to feature G while feature H arises due to second shell Y–Y, Y–Zr, and Y–Nd scattering paths. (b) The Fourier-transformed EXAFS spectra from the as-synthesized and annealed $Nd_{0.15}Y_{0.10}Zr_{0.75}O_{1.88}$ materials are shown. The intensity of feature H increases upon annealing, indicating the intermediate ordering increases occurs. The fit of the EXAFS spectra from $Nd_{0.15}Y_{0.10}Zr_{0.75}O_{1.88}$ is compared to the data in (c) R-space and (d) k-space.

Figure 11: The Fourier-transformed Y K-edge EXAFS spectra from (a) $Y_{0.25}Zr_{0.75}O_{1.88}$ and (b) $Nd_{0.20}Y_{0.05}Zr_{0.75}O_{1.88}$ materials made via co-precipitation at 800 °C and ceramic synthetic routes at 1500 °C are compared. Also included are the spectra from the materials made via the co-precipitation method annealed at 1500 °C. The spectra from the $Y_{0.25}Zr_{0.75}O_{1.88}$ made via the ceramic method and the material made via co-precipitation annealed at 1500 °C are nearly identical. Large changes in the intensities of Features G and H are observed in the spectra $Nd_{0.20}Y_{0.05}Zr_{0.75}O_{1.88}$ materials made by the different methods.

Figures

Figure 1

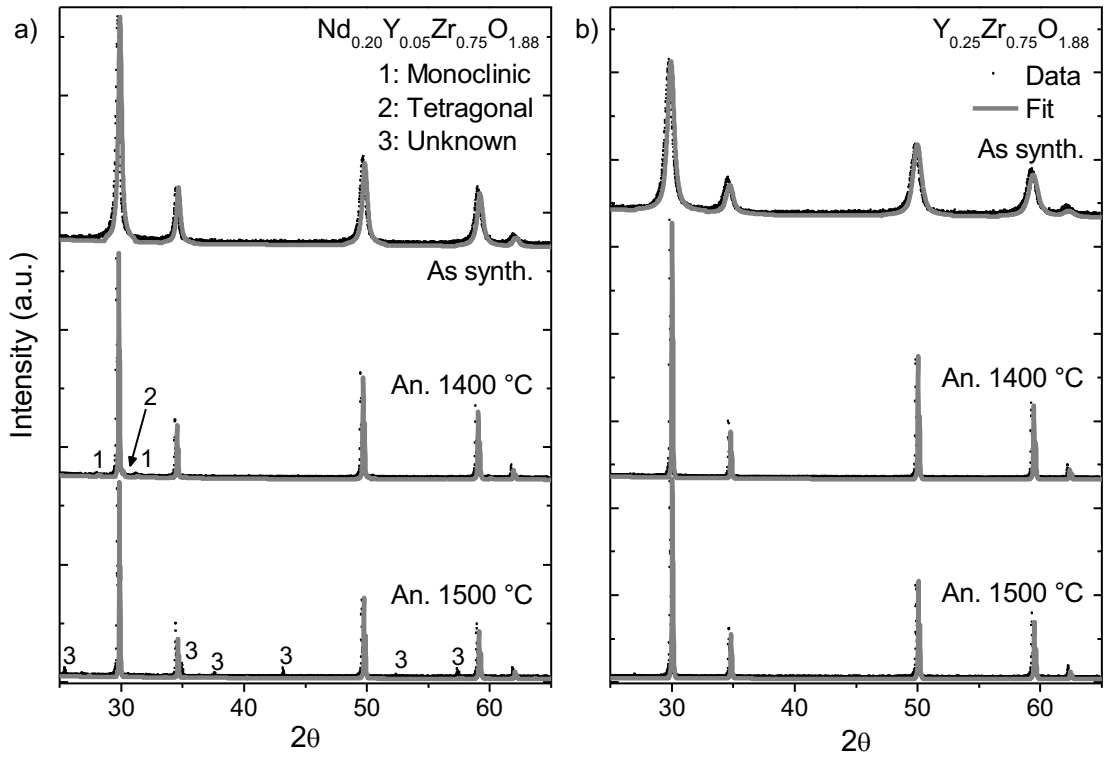

Figure 2

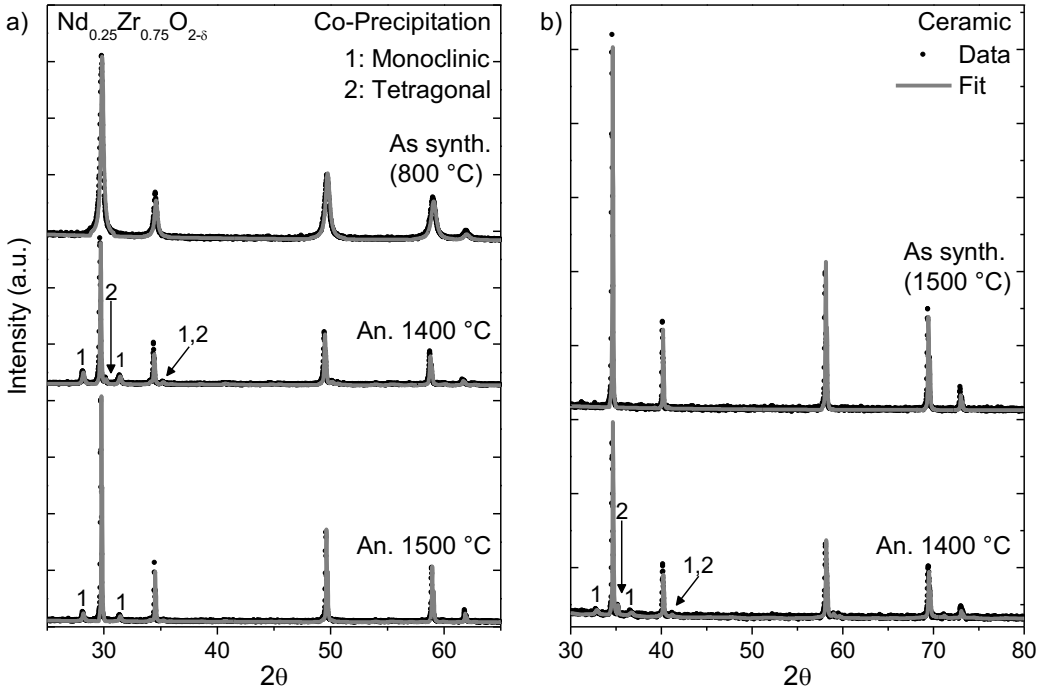
a)
$Nd_{0.25}Zr_{0.75}O_{2-\delta}$
Co-Precipitation
1: Monoclinic
2: Tetragonal
As synth.
(800 °C)
An. 1400 °C
An. 1500 °C
Intensity (a.u.)
1
2
1,2
1
1
1
30
40
50
60
2θ
b)
Ceramic
Data
Fit
As synth.
(1500 °C)
An. 1400 °C
2
1,2
1
1
30
40
50
60
70
80
2θ

Figure 3

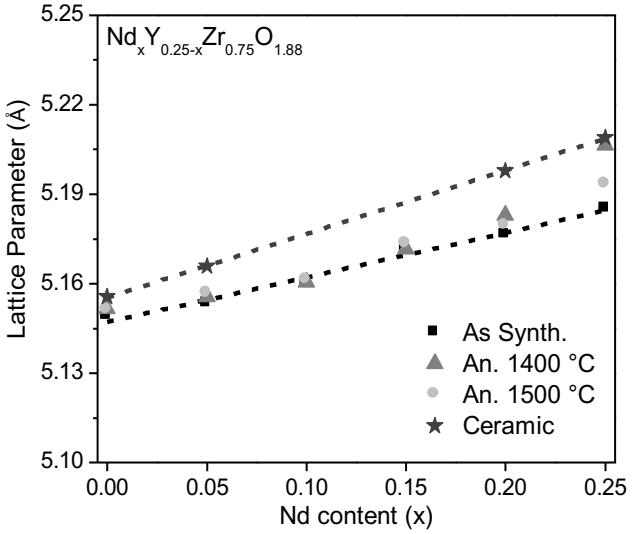
Nd$_x$Y$_{0.25-x}$Zr$_{0.75}$O$_{1.88}$
Lattice Parameter (Å)
Nd content (x)
5.25
5.22
5.19
5.16
5.13
5.10
0.00
0.05
0.10
0.15
0.20
0.25
As Synth.
An. 1400 °C
An. 1500 °C
Ceramic

Figure 4

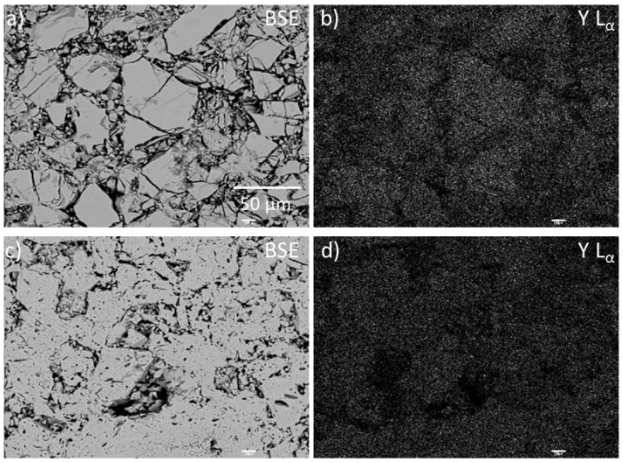

Figure 5

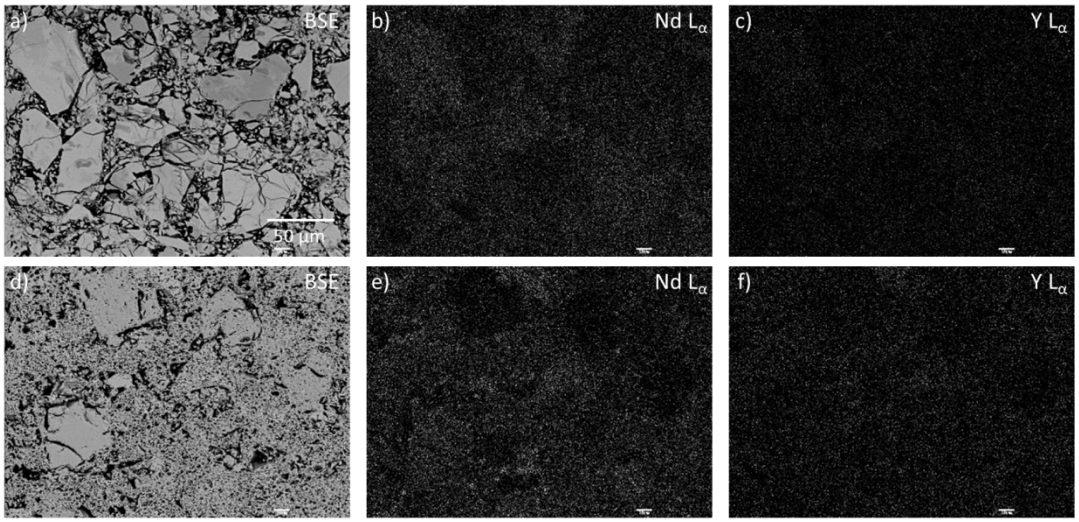

Figure 6

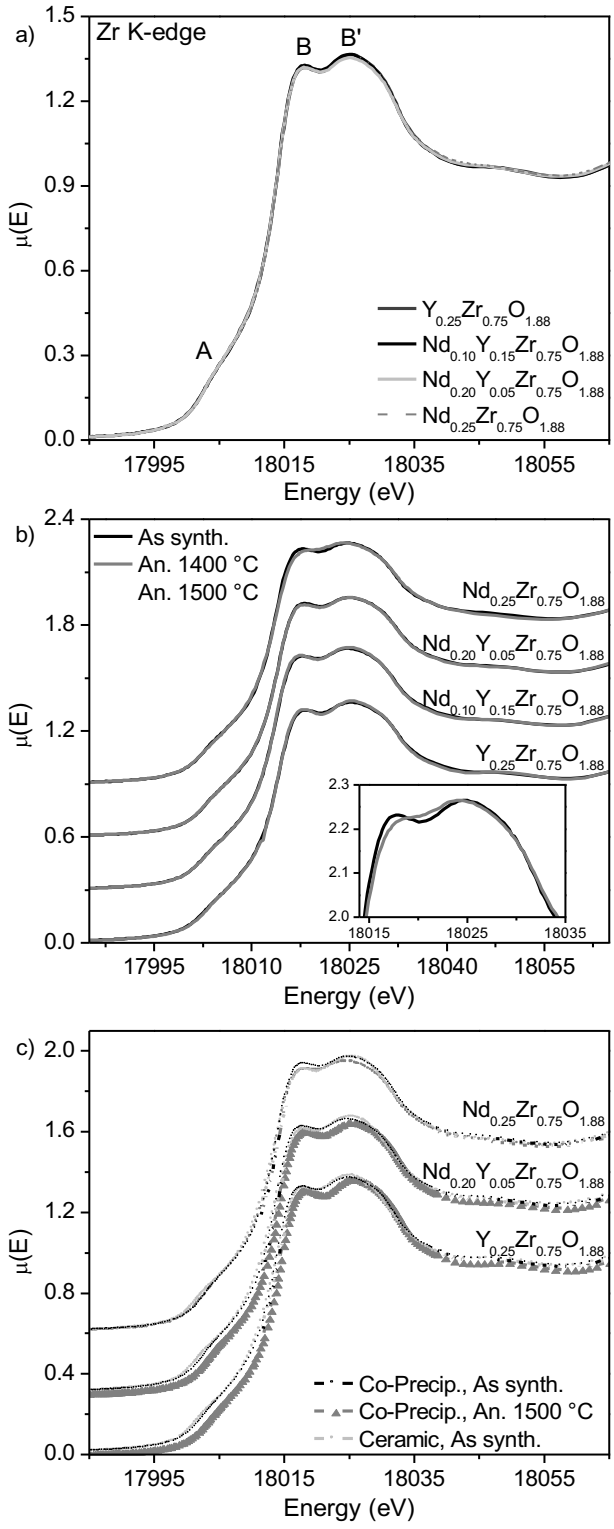
a)
Zr K-edge
A
B
B'
μ(E)
Energy (eV)
Y0.25Zr0.75O1.88
Nd0.10Y0.15Zr0.75O1.88
Nd0.20Y0.05Zr0.75O1.88
Nd0.25Zr0.75O1.88
b)
As synth.
An. 1400 °C
An. 1500 °C
c)
Co-Precip., As synth.
Co-Precip., An. 1500 °C
Ceramic, As synth.

Figure 7

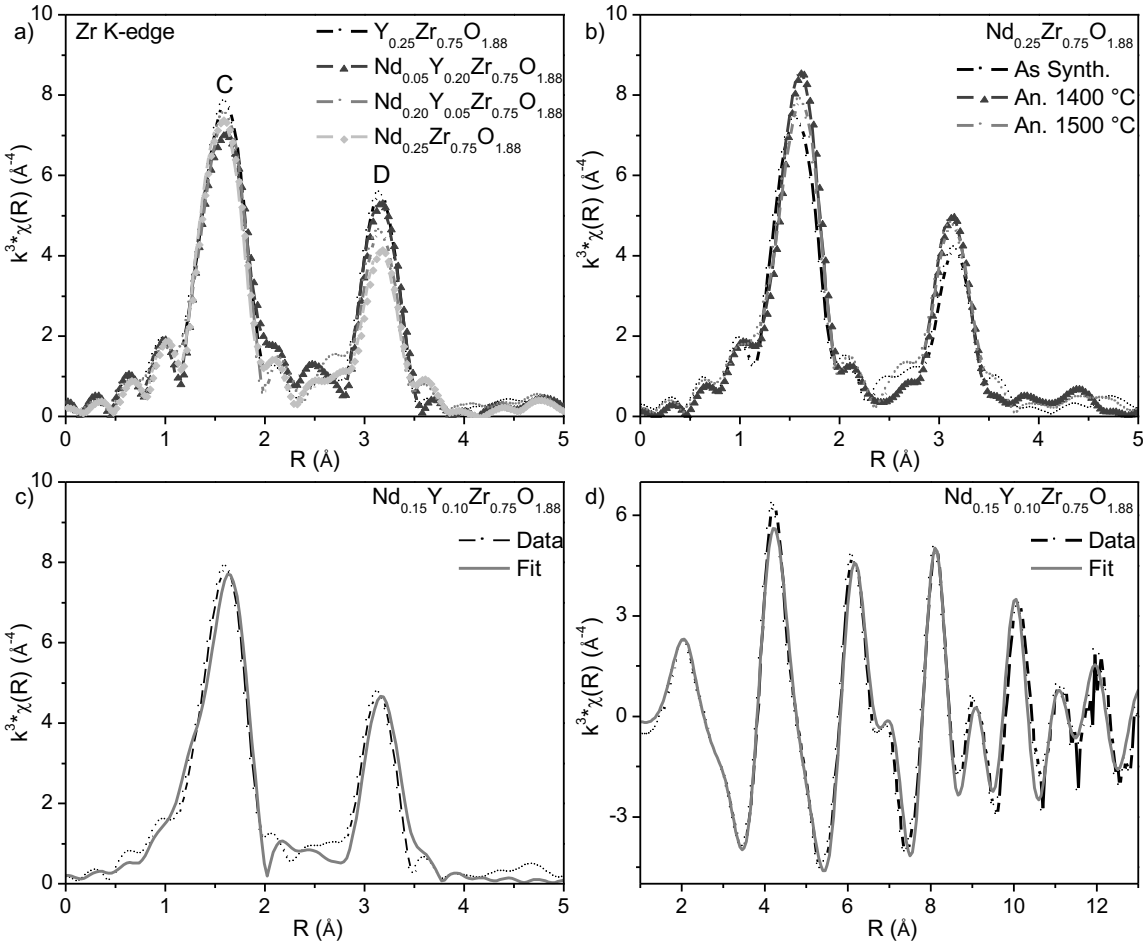
a)
Zr K-edge
$Y_{0.25}Zr_{0.75}O_{1.88}$
$Nd_{0.05}Y_{0.20}Zr_{0.75}O_{1.88}$
$Nd_{0.20}Y_{0.05}Zr_{0.75}O_{1.88}$
$Nd_{0.25}Zr_{0.75}O_{1.88}$
C
D
b)
$Nd_{0.25}Zr_{0.75}O_{1.88}$
As Synth.
An. 1400 °C
An. 1500 °C
c)
$Nd_{0.15}Y_{0.10}Zr_{0.75}O_{1.88}$
Data
Fit
d)
$Nd_{0.15}Y_{0.10}Zr_{0.75}O_{1.88}$
Data
Fit
$k^3*\chi(R)$ ($Å^{-4}$)
R (Å)

Figure 8

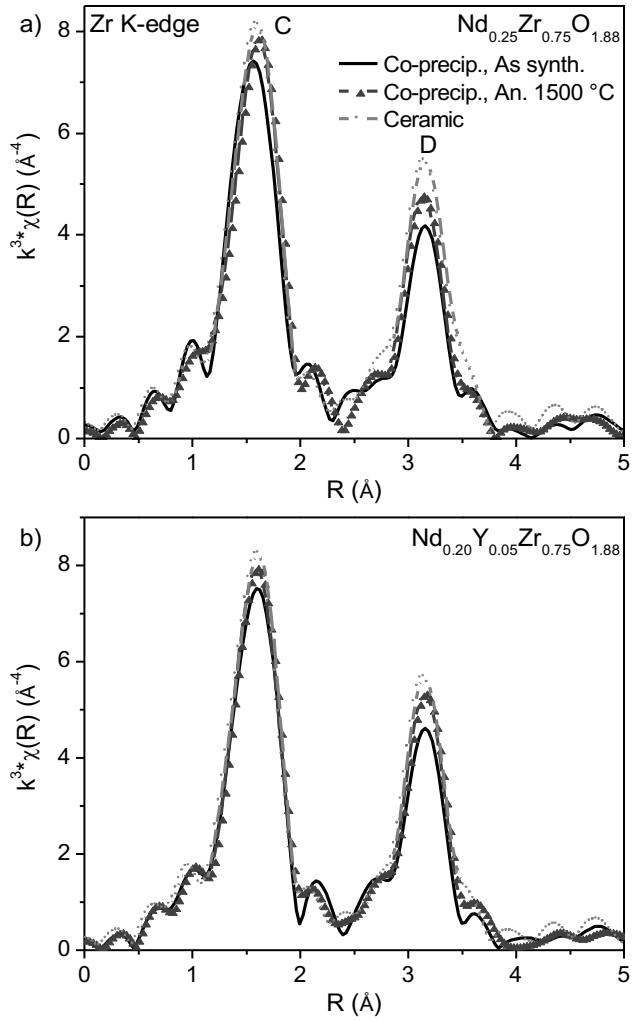
a)
Zr K-edge
C
D
$Nd_{0.25}Zr_{0.75}O_{1.88}$
Co-precip., As synth.
Co-precip., An. 1500 °C
Ceramic
$k^3*\chi(R)$ (Å^{-4})
R (Å)
b)
$Nd_{0.20}Y_{0.05}Zr_{0.75}O_{1.88}$
$k^3*\chi(R)$ (Å^{-4})
R (Å)

Figure 9

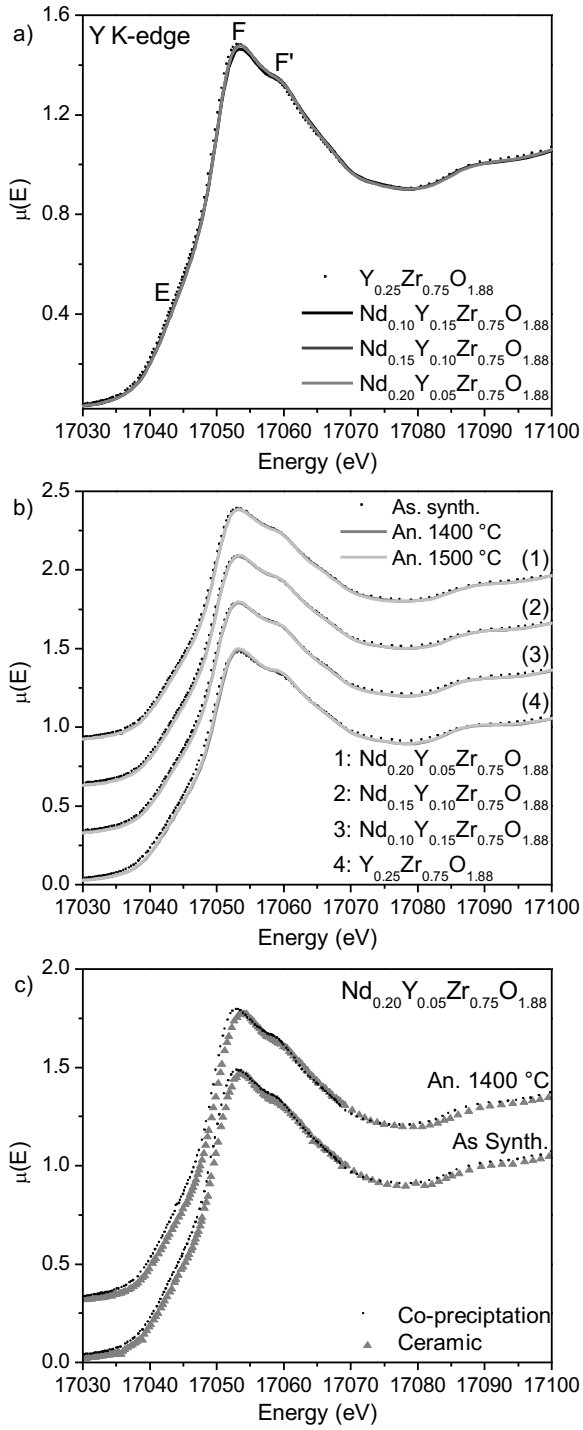
a)
Y K-edge
F
F'
E
μ(E)
Y0.25Zr0.75O1.88
Nd0.10Y0.15Zr0.75O1.88
Nd0.15Y0.10Zr0.75O1.88
Nd0.20Y0.05Zr0.75O1.88
Energy (eV)
b)
As. synth.
An. 1400 °C
An. 1500 °C (1)
(2)
(3)
(4)
1: Nd0.20Y0.05Zr0.75O1.88
2: Nd0.15Y0.10Zr0.75O1.88
3: Nd0.10Y0.15Zr0.75O1.88
4: Y0.25Zr0.75O1.88
μ(E)
Energy (eV)
c)
Nd0.20Y0.05Zr0.75O1.88
An. 1400 °C
As Synth.
Co-preciptation
Ceramic
μ(E)
Energy (eV)

Figure 10

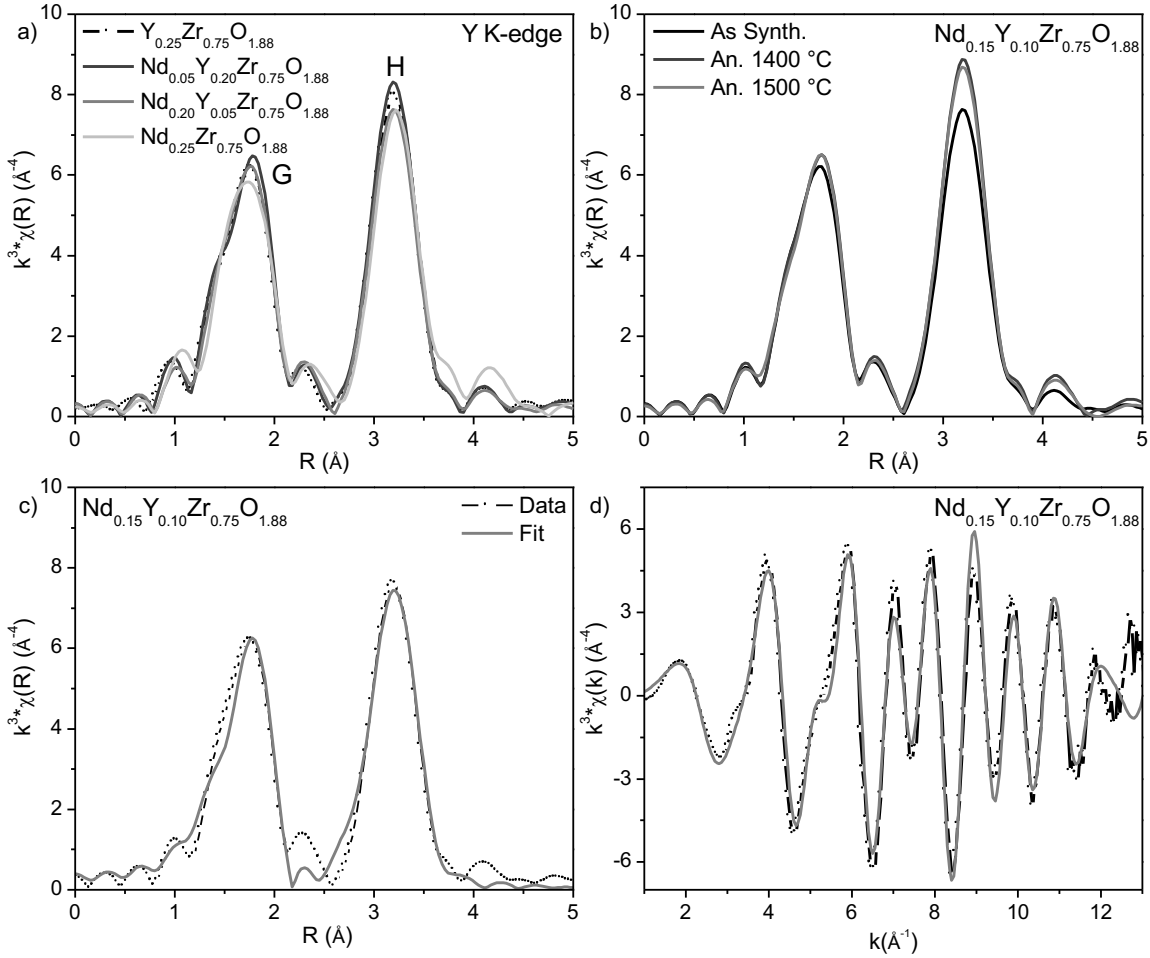
a)
Y K-edge
$Y_{0.25}Zr_{0.75}O_{1.88}$
$Nd_{0.05}Y_{0.20}Zr_{0.75}O_{1.88}$
$Nd_{0.20}Y_{0.05}Zr_{0.75}O_{1.88}$
$Nd_{0.25}Zr_{0.75}O_{1.88}$
G
H
$k^3*\chi(R)$ ($Å^{-4}$)
R (Å)
b)
As Synth.
An. 1400 °C
An. 1500 °C
$Nd_{0.15}Y_{0.10}Zr_{0.75}O_{1.88}$
c)
$Nd_{0.15}Y_{0.10}Zr_{0.75}O_{1.88}$
Data
Fit
d)
$Nd_{0.15}Y_{0.10}Zr_{0.75}O_{1.88}$
$k^3*\chi(k)$ ($Å^{-4}$)
k($Å^{-1}$)

Figure 11

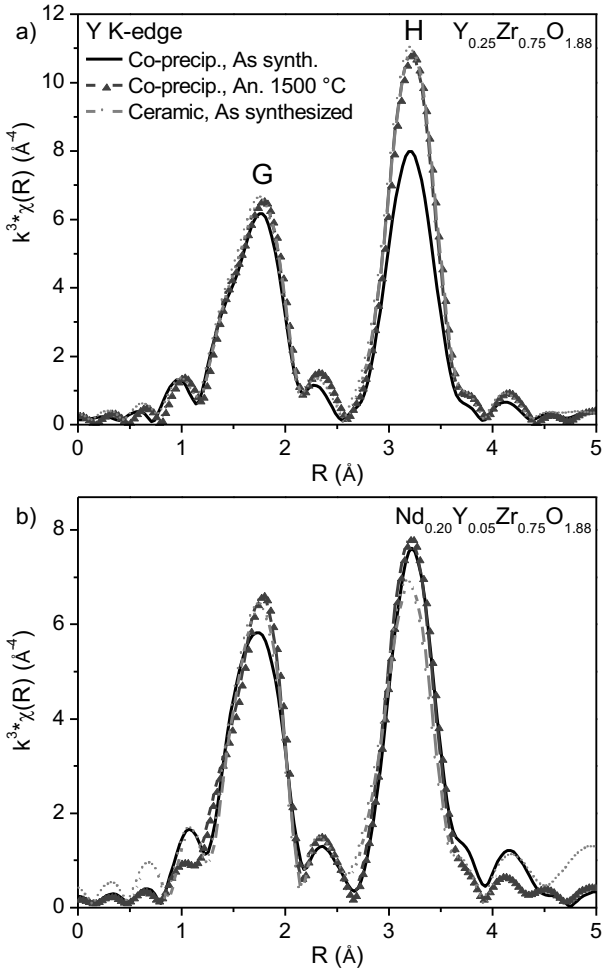
a)
Y K-edge
Co-precip., As synth.
Co-precip., An. 1500 °C
Ceramic, As synthesized
G
H
$Y_{0.25}Zr_{0.75}O_{1.88}$
$k^3*\chi(R)$ (Å^{-4})
R (Å)
b)
$Nd_{0.20}Y_{0.05}Zr_{0.75}O_{1.88}$
$k^3*\chi(R)$ (Å^{-4})
R (Å)